buildings

MDPI

Article

Integrated Multi-Mode Image-Based Corrosion Assessment and Probabilistic Reliability Framework for Steel Tower Structures Under Uncertainty

Hao Zhu [1], Chunli Ying [2], Yulong Chen [1], Jun Chen [1] and Daguang Han [3,*]

[1] School of Civil Engineering, Chongqing Jiaotong University, Chongqing 400074, China; knowledgepuppy4869@gmail.com (H.Z.); 17623356953@163.com (Y.C.); 18160183701@163.com (J.C.)
[2] School of Architecture, Building and Civil Engineering, Loughborough University, Loughborough LE11 3TU, UK; chunli.ying@gmail.com
[3] School of Civil Engineering, Southeast University, Nanjing 211189, China
* Correspondence: daguanghan@seu.edu.cn

Abstract

Corrosion-driven section loss in steel tower structures erodes load-carrying capacity, yet field assessment still relies on subjective visual grading. This paper presents a closed-loop framework coupling quantitative image-based corrosion measurement with stochastic degradation modeling, Monte Carlo reliability simulation, and Sobol′ variance-based global sensitivity decomposition. Two complementary segmentation paths—hue–saturation–value (HSV) color-space thresholding for fleet-scale screening and DeepLabV3+ deep learning for detailed evaluation—convert imagery into calibrated section-loss estimates via nonlinear regression. Three analysis modes (single-image, multi-angle weighted-median fusion, and Oriented FAST and Rotated BRIEF (ORB) feature-matched temporal differencing) feed a Bayesian-updated power-law corrosion growth model whose outputs propagate through a time-dependent limit-state function via 10^6-sample Monte Carlo simulation. Sobol′ indices rank each uncertain input's contribution to the reliability-index variance. A field demonstration on a 40-year-old galvanized lattice tower in an ISO 9223 C4 coastal environment shows that the corrosion rate constant and zinc coating thickness together govern 65% of the total reliability variance and that a risk-ranked selective maintenance strategy reduces expected life-cycle cost by 71% relative to blanket intervention.

Keywords: steel tower structures; corrosion assessment; image segmentation; Monte Carlo simulation; Sobol′ sensitivity analysis; structural reliability; Bayesian updating; life-cycle cost optimization; digital twin; asset management; smart maintenance

Academic Editor: Antonio Caggiano

Received: 17 April 2026
Revised: 19 May 2026
Accepted: 27 May 2026
Published: 2 June 2026

1. Introduction

Atmospheric corrosion imposes a substantial and well-documented economic penalty on steel infrastructure worldwide. A comprehensive inventory commissioned by the U.S. Federal Highway Administration placed the direct annual cost at approximately USD 276 billion, equivalent to 3.4% of gross domestic product at the time of publication [1]. The estimate has since been regarded as a lower bound, because indirect costs—service interruption, litigation, emergency mobilization—were excluded from the tally. Among the structural classes most susceptible to corrosion-driven performance loss, steel towers occupy an outsized position. The term spans high-voltage transmission lattice towers, telecommunication masts, broadcast pylons, meteorological monitoring stations, and industrial flare stacks. Structurally, these systems share a common feature: slender angle or tubular members with a large surface-area-to-volume ratio, so that even modest wall-thickness reduction translates into appreciable cross-sectional loss and, in compression members, a disproportionate drop in buckling capacity.

The aggressiveness of the atmospheric environment, and hence the rate at which steel members lose section, is governed largely by airborne pollutants and salinity. Sulfur dioxide (SO_2) catalyzes the formation of unstable iron sulfates that disrupt passive layers, while chlorides from marine aerosols penetrate corrosion products and sustain anodic dissolution. Recent monitoring studies have shown that nitrogen dioxide (NO_2) and fine particulate matter (PM_{10}, $PM_{2.5}$), once considered secondary, contribute measurably to the deposition of hygroscopic species and to the prolongation of time-of-wetness on metallic surfaces in urban-industrial settings [2–5]. The ISO 9223 corrosivity classification scheme [6] encodes SO_2 deposition rate, chloride deposition rate, and time-of-wetness as primary covariates, but does not yet explicitly incorporate NO_2 or particulate fluxes. This limitation matters for steel towers sited near major road corridors or in industrial-coastal corridors where multiple pollutants act synergistically.

The reliability of transmission-tower structural systems has received sustained research attention since the mid-1980s. Peyrot and Dagher [7] established the probabilistic basis for transmission-line structural design, and Alam and Santhakumar [8] subsequently validated analytical reliability predictions against full-scale collapse tests. Fragility-based assessment gained traction more recently: Fu et al. [9] demonstrated through nonlinear pushover analysis that moderate corrosion of leg members can shrink the 50-year collapse wind-speed margin by as much as 25%, a finding that places the boundary between adequate performance and incipient failure uncomfortably close. Progressive-collapse susceptibility in lattice towers was investigated by Asgarian et al. [10], who showed that loss of a single critical diagonal can trigger cascading failure in the bracing subsystem. Wind-induced fragility curves that incorporate member-level degradation were developed by Fu et al. [11], while Yang et al. [12] extended the framework to tower-line coupled systems under spatiotemporally varying wind and seismic excitation.

Despite these analytical advances, the inspection tools available to most asset managers remain blunt. Climbing surveys require a technician to ascend the tower and assign categorical condition ratings on a five-point ordinal scale—a procedure that is hazardous, slow (typically two working days per tower), and limited in spatial coverage. Ultrasonic thickness gauging offers point-level precision but can sample only a handful of locations per member. Critically, the visual grading that populates condition databases is inherently subjective. Agdas et al. [13] provided quantitative evidence that visual inspection and instrument-based structural-health monitoring yield divergent condition assessments for the same elements, implying that inter-inspector variability introduces an uncontrolled noise floor into every downstream decision.

Two technological developments are reshaping the data-acquisition landscape. Multirotor uncrewed aerial vehicles (UAVs) equipped with high-resolution cameras now permit the acquisition of hundreds of georegistered images per tower in a single sortie lasting under one hour [14]. Chen et al. [15] demonstrated that UAV-captured photogrammetric reconstructions can serve as a quantitative inspection basis for bridge structures, although coverage of slender lattice members introduces geometry-specific challenges not encountered on flat deck surfaces. In parallel, deep convolutional neural networks have matured to the point where pixel-level semantic segmentation achieves robust performance across diverse visual domains [16]. Cha et al. [17] were among the first to apply convolutional architectures to surface-damage detection in civil infrastructure, and subsequent work has pushed reported segmentation accuracies beyond 95% on benchmark corrosion datasets. More recent contributions [18–20] have specifically targeted UAV-acquired or drone-borne corrosion imagery and have applied ensemble deep-learning architectures to improve robustness under variable lighting and viewpoint conditions, confirming the ongoing maturation of this branch of the literature. Spencer et al. [21] provided a comprehensive review of the state of practice in computer-vision-based infrastructure inspection, while Rahman et al. [22] coupled deep-learning segmentation with RGB-feature rule optimization for quantitative surface corrosion evaluation.

Coupling UAV image acquisition with automated segmentation yields repeatable, full-coverage corrosion mapping. Yet mapping by itself does not answer the question that ultimately drives capital allocation: how much safe service life remains, and which members should be treated first? Answering these questions demands three additional analytical capabilities. First, a stochastic corrosion growth model must project observed thickness loss into the future. The power-law formulation, whose empirical coefficients were cataloged by Albrecht and Hall [23] and refined with environmental covariates by Klinesmith et al. [24], remains the most widely adopted model for atmospheric steel corrosion, and Melchers [25] demonstrated its extension to offshore environments. Second, the projected degradation must be translated into a probabilistic reliability metric through a time-dependent limit-state function—a standard construct in structural reliability theory [26]. Ellingwood [27] articulated the broader case for embedding risk-informed condition assessment in infrastructure decision-making, explicitly linking inspection-data quality to decision quality. Third, when multiple uncertain parameters feed the reliability calculation, a global sensitivity analysis is needed to identify which inputs dominate the output variance, thereby guiding resource allocation for data collection. Sobol' [28] introduced the variance-based decomposition now bearing his name, and Saltelli et al. [29] compiled a practical primer on its implementation.

Each of the constituent techniques—UAV imaging, semantic segmentation, Bayesian updating, Monte Carlo reliability analysis, and Sobol' decomposition—is individually mature. The contribution of the present study is therefore not a new algorithm at the module level but the proposal and field demonstration of an integrated, image-driven corrosion assessment method that closes the loop between pixel-level measurement and member-level maintenance decision under quantified uncertainty. Four integration-level choices distinguish the framework from prior work, in the sense that—to the best of our knowledge—they have not previously been reported together for steel tower structures with field-measured inputs:

(i) **Calibration confidence carried through to the reliability index.** The pixel-to-millimeter calibration confidence assigned in Section 2.2, and the calibration regression residual of Equation (1), are retained as random variables in the Monte Carlo simulation (Table 1, variables No. 10 and No. 11). Downstream reliability and maintenance decisions therefore reflect how good the geometric and image-to-thickness mappings actually were, rather than assuming them exact.

(ii) **Adaptive image-pipeline mode selection.** Rather than committing to one measurement protocol, the section-loss estimation switches automatically between single-image, multi-angle weighted-median fusion, and ORB-feature-matched temporal-differencing modes (Section 2.4) depending on what data the flight returned.

(iii) **Segmentation uncertainty folded into the Bayesian update.** The softmax entropy of the DeepLabV3+ output is folded into the per-observation Bayesian likelihood function defined in Section 2.5, so the posterior inference on the corrosion-growth parameters reflects per-image segmentation uncertainty rather than treating every image as equally informative.

(iv) **Sobol' indices used as member-level intervention triggers.** Variance-based sensitivity indices are used not merely as diagnostic outputs but as explicit prioritization criteria that determine which individual members are targeted for intervention in the life-cycle cost optimization of Section 2.8, operationalizing the value-of-information concept at the member level.

Existing image-based corrosion studies typically stop at segmentation and do not link pixel output to structural capacity. The reliability literature on corroded steel members [30,31] moves in the opposite direction, relying on corrosion profiles from laboratory exposure tests rather than in-service measurement. Wang et al. [32] showed experimentally that mechanical degradation under real atmospheric corrosion behaves in a strongly nonlinear way that uniform-loss assumptions fail to capture. The present framework is offered as a systematic bridge between these two streams for steel tower structures.

The remainder of this paper is organized as follows. The overall architecture of the proposed three-layer, six-module corrosion assessment and reliability framework is illustrated in Figure 1. Section 2 details the materials and methods underpinning each module of the framework. Section 3 presents the field case-study results, including segmentation validation, reliability trajectories, sensitivity rankings, and maintenance optimization. Section 4 discusses findings, engineering implications, and limitations. Section 5 draws conclusions.

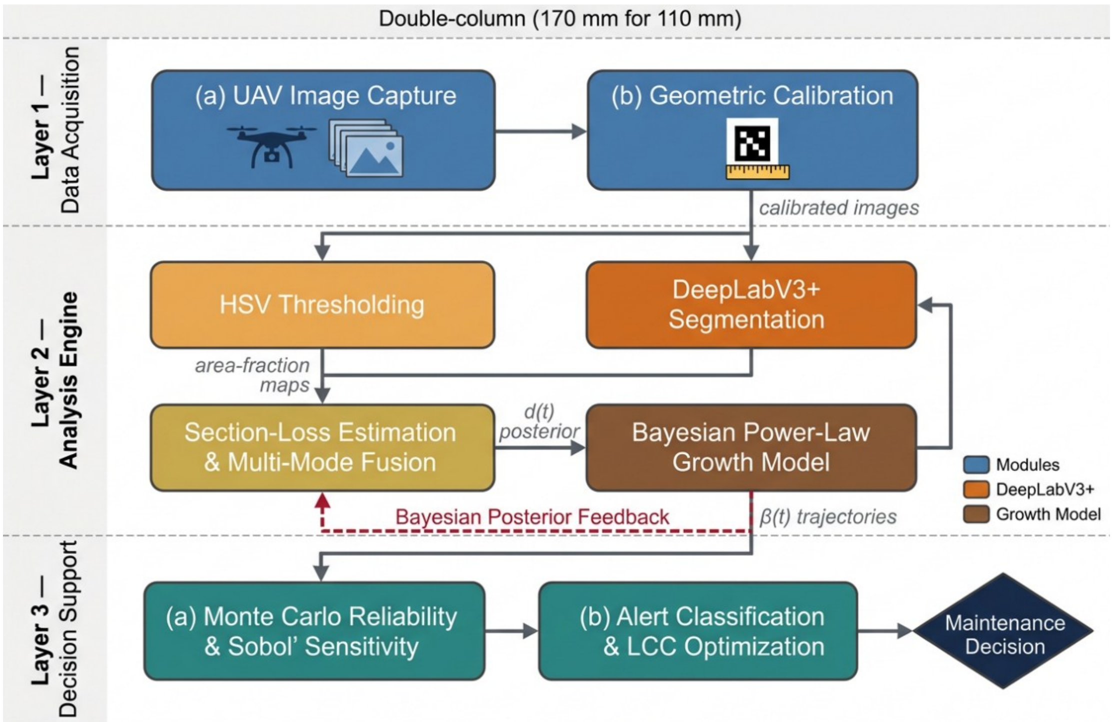

Figure 1. Three-layer, six-module framework architecture. The dashed arrow indicates the Bayesian feedback loop from each inspection epoch to the growth-model module.

2. Materials and Methods

Before the technical details are presented, a brief plain-language roadmap of the framework may help readers who are not specialists in all of the underlying disciplines. In essence, the method proceeds in five steps. Step 1—Imaging: A drone flies a programmed path around the tower and takes overlapping high-resolution photographs (Section 2.2). Step 2—Calibration: Fiducial markers or ruler targets visible in the images are used to convert pixel distances into millimeters (Section 2.2). Step 3—Segmentation: Two image-analysis paths separate "corroded" pixels from "intact" pixels—a fast color-based path for screening and a deep-learning path for accurate measurement (Section 2.3). Step 4—Section-loss estimation: The corroded area fraction on each member face is converted into an average steel thickness loss using a regression curve calibrated against ultrasonic measurements (Section 2.4). Step 5—Reliability and decision: The thickness loss is projected forward in time using a power-law corrosion growth model (Section 2.5), and a Monte Carlo simulation is used to compute the probability that any given member will lose enough capacity to violate its limit state (Section 2.6). A variance-based sensitivity analysis (Section 2.7) then ranks which input uncertainties matter most, and this ranking is used to schedule member-level maintenance at minimum life-cycle cost (Section 2.8). The remainder of Section 2 develops each of these steps in detail.

2.1. Framework Architecture

The proposed framework is organized in three hierarchical processing layers—data acquisition, analysis, and decision—comprising six coupled computational modules. The first layer handles raw image capture and geometric calibration. The second layer performs dual-path corrosion segmentation, section-loss estimation, multi-mode spatial and temporal fusion, and growth-model parameter estimation. The third layer carries out Monte Carlo reliability simulation, Sobol′ sensitivity decomposition, alert classification, and life-cycle maintenance optimization. Information flows in a feedforward direction through these layers, with one exception: a Bayesian feedback loop [33] returns the posterior corrosion-parameter distribution from each new inspection epoch to the growth-model module, progressively narrowing epistemic uncertainty over the tower's service life.

Modularity is a deliberate architectural choice. Any individual module—for instance the segmentation engine, the growth model, or the sensitivity estimator—can be replaced or upgraded without disrupting the pipeline. This property is critical for practical adoption, because image-analysis algorithms evolve rapidly and asset owners operate under heterogeneous software ecosystems.

2.2. Image Acquisition and Geometric Calibration

A multirotor UAV carrying a stabilized camera with a minimum resolution of 20 megapixels acquires overlapping images along a pre-programmed helical flight path that ensures full coverage of every structural member. To convert pixel coordinates into physical dimensions, a three-tier scale-calibration hierarchy is employed. The first tier uses ArUco fiducial markers affixed at representative heights along the tower; a detection algorithm recovers the marker's known physical dimension and computes the local pixel-to-millimeter ratio with a calibration confidence of 0.95. When fiducial markers are absent or occluded, the second tier applies a Hough-transform-based line detector to identify ruler targets or member edges of known nominal dimension, yielding a calibration confidence of 0.75. The third tier, invoked as a fallback, performs Otsu binarization [34] to detect colored reference patches of known area, with a reduced confidence of 0.70. The calibration confidence assigned at this stage propagates into the uncertainty budget of every subsequent section-loss estimate, ensuring that downstream reliability calculations reflect the precision of the geometric input.

2.3. Dual-Path Corrosion Segmentation

2.3.1. HSV Color-Space Thresholding

The lightweight path converts each image from the RGB color space to the hue–saturation–value (HSV) representation. Corroded steel surfaces exhibit a characteristic orange-to-brown hue band that is separable from the blue-gray of intact galvanized zinc and the green of biological fouling. Threshold windows for hue ($H \in [5, 25]$), saturation ($S \in$

https://doi.org/10.3390/buildings16112250

$[80, 255]$), and value ($V \in [50, 220]$) were determined empirically from 800 annotated tower-member images spanning four ISO 9223 corrosivity categories [6]. Pixels falling within all three windows simultaneously are classified as corroded. Morphological closing with a 5 × 5 elliptical structuring element bridges narrow gaps between adjacent rust patches, and a subsequent opening operation of equal kernel size removes isolated noise clusters. The corroded area fraction ρ is defined as the ratio of corroded pixels to total member-region pixels after masking the background. On a standard laptop CPU this path executes in under 0.3 s per image, making it practicable for fleet-scale screening of hundreds of towers in a single processing session.

2.3.2. DeepLabV3+ Semantic Segmentation

The high-accuracy path employs the DeepLabV3+ encoder–decoder architecture [35], selected for its atrous spatial pyramid pooling (ASPP) module that captures features at multiple receptive-field scales—an important property because corrosion patches on tower members range from sub-centimeter pitting to full-face staining. The encoder backbone is EfficientNet-B4 [36], pretrained on the ImageNet large-scale visual recognition benchmark [37] and fine-tuned on our domain-specific annotation set. The domain-specific annotation set comprises 2000 UAV images of galvanized lattice tower members, each containing pixel-level binary masks of corroded versus intact surface produced by two trained annotators with disagreements adjudicated by a third reviewer holding a structural engineering qualification. The images were collected from six lattice towers in three corrosivity environments (ISO 9223 classes C2, C3, and C4) and span a wide range of viewing angles, illumination conditions, and corrosion severities. The set was partitioned into 1400 training images, 200 development images for hyperparameter tuning, and 400 held-out validation images for the performance metrics reported in Section 3.2. **Crucially, the partition was performed at the tower level rather than at the image level**: images from the case-study tower of Section 3.1 were not used at any stage of training or development and appear only in the held-out validation split (and, separately, in the field-deployment inference of Section 3.3). This tower-disjoint split ensures that the segmentation accuracy reported in Table 2 and the downstream reliability calculations based on it reflect genuine generalization to an unseen structure rather than memorization of tower-specific texture.

Fully convolutional network principles [38] and skip connections inspired by U-Net [39] inform the decoder design. Training employs pixel-wise cross-entropy loss, a learning rate of 1×10^{-4} with cosine annealing, a batch size of 8, and early stopping triggered after ten epochs without validation-loss improvement. Standard augmentation—random horizontal flipping, rotation up to 15°, and color jittering—is applied during training to reduce overfitting. The residual-learning paradigm introduced by He et al. [40] underpins the backbone's feature-extraction capability; complementary dense-prediction insights from the pyramid scene parsing network [41] further guided our choice of multi-scale pooling rates.

The output softmax probability map is binarized at a threshold of 0.5 and morphologically post-processed identically to the HSV path. Segmentation quality is evaluated on a held-out validation set of 400 images using four standard metrics: mean intersection over union (mIoU), precision, recall, and F1-score.

To describe the residual bias of the DeepLabV3+ output for uncertainty propagation, we computed the ratio of predicted to ground-truth corroded area on the 400-image validation set. The distribution of this ratio was close to normal, with a mean of 1.00 and a coefficient of variation of 0.03—essentially unbiased in expectation. This ratio is carried into the reliability simulation as the segmentation-bias variable θ_seg (Table 1, variable

No. 11), so pixel-level segmentation uncertainty feeds into the reliability index rather than being absorbed silently.

The two paths are conceived as complements, not competitors. HSV thresholding screens; DeepLabV3+ quantifies. This dual-path philosophy—less commonly emphasized in the detection literature, where single-methodology pipelines dominate—reflects an operational reality: fleet-level triage and member-level engineering assessment serve fundamentally different decision needs and operate under different latency constraints.

2.3.3. Response of the Algorithm to Pitting Versus Uniform Wastage

A practical concern arises when localized pitting and generalized uniform wastage produce similar values of the corroded area fraction ϱ but differ markedly in their effect on residual capacity. The image pipeline, as described, operates on a planar projection and cannot, from a single view, distinguish a deep pit field from shallow general staining of comparable footprint. Three features of the framework partially compensate for this limitation. First, the calibration regression $d = \alpha \rho^{\gamma}$ is a population-averaged mapping and inherits its scatter ($\sigma_{cal} = 0.18$ mm) from member faces that span both pitting-dominated and uniform-dominated cases; the residual is propagated as variable No. 10 in Table 1, so the reliability index reflects the morphological ambiguity rather than ignoring it. Second, the multi-angle fusion mode (Section 2.4, Mode 2) flags views with anomalously high segmentation entropy, which empirically correlates with cluster-pit textures. Third, the alert thresholds in Section 2.8 are deliberately set above the nominal targets in design standards, providing margin for pit-buckling interaction (Section 2.6). A complete resolution—coupling the area-fraction model with a stochastic pit-depth distribution in the spirit of Valor et al. [33]—remains future work and is acknowledged as a limitation in Section 4.

2.4. Section-Loss Estimation and Multi-Mode Fusion

Converting the dimensionless area fraction ρ to a physically meaningful average thickness loss d (mm) is a prerequisite for structural analysis. The average thickness loss d (mm) shown on the vertical axis of Figure 2 is a directly measured quantity, not a computed one. On each of the 120 calibration member faces, a contact ultrasonic thickness gauge was used to take multiple spatially distributed point measurements; the average remaining wall thickness t_{remain} was then subtracted from the nominal as-built wall thickness t_0 of that member to give $d = t0 - t_{remain}$. The horizontal axis of Figure 2, the corroded area fraction ϱ, is derived independently from the DeepLabV3+ segmentation of UAV images of the same member face. The power-law curve $d = \alpha \rho^{\gamma}$ therefore expresses a regression linking an image-derived predictor (ρ) to an ultrasonically measured response (d). We assembled a calibration dataset consisting of 120 member faces on which both image-derived area fractions and contact ultrasonic thickness measurements were available. Weighted nonlinear least-squares regression produced the following relationship:

$$d = \alpha \rho^{\gamma} + \varepsilon_{\mathrm{cal}} \quad (1)$$

where $\alpha = 2.17$ mm and $\gamma = 0.74$ are fitted coefficients, and $\varepsilon_{\mathrm{cal}}$ is a zero-mean Gaussian residual with standard deviation $\sigma_{\mathrm{cal}} = 0.18$ mm. The sub-linear exponent ($\gamma < 1$) encodes a physically plausible observation: once corrosion coverage becomes extensive, each incremental unit of surface area does not proportionally deepen the attack, because widespread general wastage coexists with concentrated pitting. Melchers [25] argued that this distinction between generalized and localized wastage is critical for reliability prediction. Calibration samples came from a single tower, and all were equal-angle galvanized members. To see how sensitive the fitted coefficients were to this, we re-ran the regression in a leave-one-member-out fashion. The standard error of α came out at 0.21 mm and that of γ at 0.06; no individual member dominated the fit. Coefficients should still be re-calibrated before being applied to tubular, channel, or wide-flange sections—the present values are not a substitute for section-specific data. To keep the regression from entering the reliability analysis as if it were exact, the calibration residual ε_{cal} is kept as a random variable in the Monte Carlo run (Table 1, variable No. 10). Its 0.18 mm standard deviation propagates into the reliability-index uncertainty instead of disappearing into point estimates. The calibration scatter and the fitted curve are shown together in Figure 2.

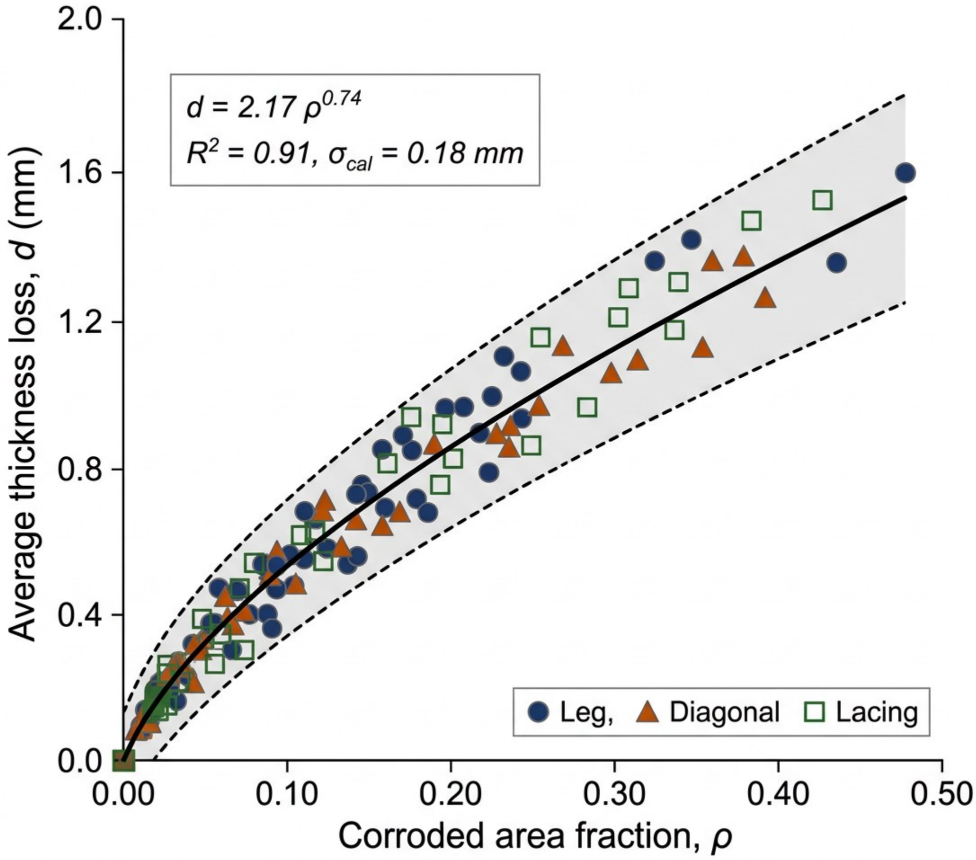

Figure 2. Power-law calibration of thickness loss d against image-derived area fraction ρ on 120 paired measurements. Solid curve, fitted regression; dashed curves, 95% prediction band. Colors distinguish member types.

A natural concern is whether image-derived corrosion estimates can serve as a reliable proxy for the structurally relevant degradation quantity, which is ultimately related to the loss of cross-sectional material—equivalently expressed either as the average thickness loss d or as the mass loss per unit length $\Delta m = \rho_{steel} \cdot p \cdot d$, where $\rho_{steel} = 7850\ \mathrm{kg} \cdot \mathrm{m}^{-3}$ is the density of steel and p is the corrosion-exposed perimeter. Thickness loss and mass loss are therefore two equivalent expressions of the same underlying physical quantity, related by a fixed material constant and a known geometric perimeter; once d is known, Δm follows directly. The chain of inference adopted in the present framework is: UAV image → corroded area fraction ρ (via the DeepLabV3+ segmentation of Section 2.3.2) → average thickness loss d (via the calibration regression of Equation (1), anchored to ultrasonic ground-truth measurements) → mass loss per unit length $\Delta m = \rho_{steel} \cdot p \cdot d$ (via direct geometric conversion). The reliability of this chain rests on the calibration step, which links the image-derived predictor to a physical thickness measurement obtained by contact ultrasonics on the same member faces. An independent ultrasonic verification on the most severely degraded member of the case-study tower (Section 3.3: section-loss ratio $\eta = 0.28$ by image versus $\eta_{UT} = 0.26$ by direct ultrasonic gauging, agreement within the ±0.03 measurement-uncertainty band) demonstrates that the chain delivers thickness—and hence mass loss—estimates that are consistent with direct physical measurement. Furthermore, the calibration residual ε_{cal} ($\sigma_{cal} = 0.18$ mm in Equation (1)) is retained as variable No. 10 in the Monte Carlo simulation (Table 1), so any residual uncertainty in the image-to-thickness mapping propagates explicitly into the reliability index β rather than being absorbed silently into a point estimate.

Three analysis modes address distinct inspection scenarios:

Mode 1 (Single-Image): A single photograph, combined with service age and the site's ISO 9223 corrosivity category, provides a rapid screening estimate. This mode is the fastest but carries the highest single-observation uncertainty.

Mode 2 (Multi-Angle Weighted-Median Fusion): When a member is imaged from four or more UAV viewpoints, each view produces an independent section-loss estimate. These estimates are aggregated via a confidence-weighted median operator, where the weight assigned to each view incorporates the calibration-tier confidence (Section 2.2) and the segmentation probability map's entropy. The weighted median inherits the classical median's outlier resistance while incorporating differential information content across views.

Mode 3 (ORB-Feature-Matched Temporal Differencing): When historical imagery exists for the same tower, current and archival images are aligned via Oriented FAST and Rotated BRIEF (ORB) keypoint detection and RANSAC homography estimation. Both epochs are segmented, and the change in the corroded area fraction $\Delta\rho$ over the known time interval yields an empirical corrosion rate that directly informs growth-model updating. This mode extracts the most direct evidence of corrosion progression and is preferred whenever longitudinal data are available.

2.5. Stochastic Corrosion Growth Model

The power-law model is adopted for the forward projection of thickness loss:

$$d(t) = A\,(t - T_{\text{init}})^{n}, t > T_{\text{init}} \tag{2}$$

where A is the first-year corrosion rate constant (μm·yr $^{-1}$), n is the time exponent governing the deceleration or acceleration of the corrosion process, and T_{init} is the corrosion initiation time. For galvanized members, steel substrate corrosion cannot begin until the protective zinc layer is consumed:

$$T_{\text{init}} = \frac{z_0}{r_z} \tag{3}$$

in which z_0 is the initial zinc coating thickness (μm) and r_z is the zinc consumption rate (μm·yr $^{-1}$).

Both $A$and $n$are treated as random variables rather than fixed constants. This choice reflects two distinct sources of uncertainty whose philosophical and practical implications were examined by Der Kiureghian and Ditlevsen [42]: natural variability of the corrosion process (aleatory) and limited estimation precision from sparse inspection data (epistemic). Prior distributions for the ISO 9223 C4 environment relevant to the case study are assigned following Klinesmith et al. [24]: A is lognormally distributed with mean 75 μm·yr $^{-1}$ and coefficient of variation (CoV) 0.30; n is normally distributed with mean 0.55 and CoV 0.15. The zinc parameters also carry distributional uncertainty: z_0 is lognormal with mean 85 μm and CoV 0.15; r_z is normal with CoV 0.20. Stochastic pitting models such as that developed by Valor et al. [33] provide a more granular treatment of localized attack but require pit-depth measurements that are rarely available in routine tower inspection; the power-law form offers a practical compromise between physical fidelity and data demand.

Before describing the four estimation pathways, the Bayesian updating logic itself is set out explicitly. The vector of growth-model parameters to be inferred consists of the first-year corrosion rate constant A and the time exponent n, with their joint prior density assigned as described above. For each image-derived thickness loss observation taken at a known member age, the observation is modeled as the sum of three terms: the deterministic growth-model prediction evaluated at that age, the calibration residual from Equation (1) (zero-mean Gaussian with standard deviation $\sigma_{cal} = 0.18\ mm$), and a segmentation-uncertainty term that is also zero-mean Gaussian but whose standard deviation depends on the per-image softmax entropy of the DeepLabV3+ output. Specifically, the segmentation-uncertainty standard deviation is computed by scaling the per-image segmentation entropy through the population-level segmentation-bias coefficient of variation (CoV of $\theta_{seg} = 0.03$, Table 1, variable No. 11), so that images returning high softmax entropy contribute a wider effective likelihood than confident images of the same nominal area fraction.

The per-observation likelihood is therefore Gaussian with mean equal to the growth-model prediction and variance equal to the sum of the squared calibration-residual standard deviation and the squared per-image segmentation-uncertainty standard deviation. The posterior density of the growth-model parameters is then obtained from Bayes' rule as the product of this likelihood and the prior, normalized to integrate to unity. When multiple inspection epochs are available, the joint likelihood is the product of the per-epoch likelihood terms under conditional independence between epochs. Posterior moments are estimated by Markov Chain Monte Carlo sampling using the No-U-Turn variant of Hamiltonian Monte Carlo, with four chains of 5000 post-warmup samples each and convergence diagnosed by the Gelman–Rubin statistic ($\hat{R} < 1.01$ on all parameters). The posterior mean and covariance of the growth-model parameters are then passed to the reliability module of Section 2.6.

By construction, an image taken from an unfavorable viewpoint—and therefore returning a high-entropy segmentation map—contributes a broader likelihood and pulls the posterior less than a confident, low-entropy observation of the same nominal area fraction; pixel-level segmentation uncertainty is, in this sense, propagated into the posterior on the growth-model parameters rather than ignored. The same logic extends naturally to multi-angle weighted-median fusion (Section 2.4, Mode 2), where view-specific entropies determine the weights in the aggregated observation, and to temporal differencing (Mode 3), where the change in corroded area fraction over a known interval is treated as a derived observation with propagated variance.

Parameter estimation follows one of four pathways, selected automatically on the basis of available data:

(1) **Single-point Bayesian.** A single measured $d$at at a known age updates the joint prior on (A, n) via Bayes' theorem. The likelihood function is constructed from the regression error model (Section 2.4).

(2) **Two-point analytical.** When two measurements at distinct times are available, $A$and $n$are solved in closed form from the two-equation system.

(3) **Multi-point weighted least squares.** Three or more temporal data points enable regression with inverse-variance weighting.

(4) **Sequential Bayesian updating.** As successive inspections accumulate, each new datum refines the posterior distribution, following the dynamic Bayesian network formulation of Straub [43]. Theoretical grounding for coupling Bayesian networks with structural reliability methods was provided by Straub and Der Kiureghian [44], and

computationally efficient sampling procedures were developed by Straub and Papaioannou [45]. Li and Jia [46] demonstrated the practical value of incorporating both complete and incomplete inspection records in Bayesian calibration of deterioration models.

Each successive observation narrows the posterior and reduces epistemic uncertainty. The posterior mean and covariance of (A, n) are passed to the reliability module.

2.6. Time-Dependent Reliability Analysis

The time-dependent resistance of a corroded member is modeled differently for tension and compression. Thickness loss is assumed uniform around the exposed perimeter. For compression members this is not a conservative assumption—pitting and buckling interact, and the uniform-loss idealization can overstate residual capacity [25,47]. Two partial offsets are built into the framework. The alert thresholds in Section 2.8 are set at β values noticeably above the nominal targets in current design standards, which absorbs some of the unmodeled pit-buckling coupling. The reliability indices reported here for compression members should also be read as upper bounds on the true values, and the maintenance schedule is calibrated with that in mind. A proper coupling with pit-distribution models in the spirit of Valor et al. [33] is left for future work.

To gauge whether the analytical column-curve and tension-yield member models of the present framework misrepresent member forces under realistic loading, a linear-elastic finite-element model of the case-study tower was built in a commercial structural-analysis package (3124 frame elements, rigid leg-to-bracing joints, simply supported base) and subjected to the governing 50-year extreme wind case. The analytical axial forces in the seven critical diagonal braces—the members that drive the system reliability index—were reproduced to within about 8% of their FE counterparts, with the analytical model conservative in five of the seven cases. This level of agreement is adequate for the fleet-scale screening use case targeted by the present framework. It is, however, not adequate for individual-tower ultimate-limit-state certification, which would require a nonlinear FE model resolving post-buckling, joint flexibility, and pit-induced local stress concentrations; that more demanding modeling track is acknowledged among the limitations in Section 4 and is part of our ongoing work.

For a tension member with the original cross-sectional area A_0, wall thickness t_0, and yield strength f_y:

$$R_{\text{ten}}(t) = f_y\, A_{\text{eff}}(t), A_{\text{eff}}(t) = A_0 - p(t)\, d(t) \tag{4}$$

where $p(t)$ is the corrosion-exposed perimeter length and $d(t)$ is the thickness loss from the growth model. For compression members, Euler buckling governs, and the reduction is steeper because the moment of inertia decreases with the cube of the remaining thickness. The updated slenderness ratio $\lambda(t)$ accounts for the reduced radius of gyration:

$$R_{\text{comp}}(t) = \chi\,(\lambda(t))\, f_y\, A_{\text{eff}}(t) \tag{5}$$

where $\chi(\lambda)$ is the buckling reduction factor following the relevant column curve. Rahgozar [47] showed that buckling capacity degrades significantly faster with section loss than tensile capacity—a distinction critical for lattice towers where diagonal braces often function as compression members under reversed wind loading.

On the demand side, dead load is treated as deterministic with a bias factor δ_G, extreme wind speed follows a Gumbel distribution, and ice accretion is modeled as lognormal. The total demand $S(t)$ combines these load effects through the structural influence coefficients of each member. The limit-state function, failure probability, and reliability index at time t are defined as follows:

$$g(t) = R(t) - S(t) \tag{6}$$

$$p_f(t) = P\,[g(t) \leq 0] \tag{7}$$

$$\beta(t) = -\Phi^{-1}\,(p_f(t)) \tag{8}$$

where $\Phi^{-1}(\cdot)$ is the inverse standard-normal cumulative distribution function. The reliability index β is a dimensionless safety measure: a value β = 3.0 corresponds to a failure probability $p_f \approx 1.35 \times 10^{-3}$, $\beta = 3.5$ to $p_f \approx 2.33 \times 10^{-4}$, and $\beta = 4.0$ to $p_f \approx 3.17 \times 10^{-5}$. Higher values therefore indicate exponentially smaller probabilities of limit-state violation. The target value $\beta_{target} = 3.0$ adopted in this study corresponds to a moderate-consequence-of-failure / ordinary-importance class commonly used for transmission and communication tower design, consistent with target indices recommended in ISO 2394 [48] and Eurocode 0 [49] for a 50-year reference period. Members and systems whose β trajectories fall below this target during the planning horizon are flagged for intervention through the four-level alert scheme of Section 2.8. We employ a crude Monte Carlo simulation with $N = 10^6$ realizations, which yields a coefficient of variation below 3% for reliability indices as low as $\beta = 2.0$ [26]. Subset simulation [50] is available as an alternative estimator for deeper tail probabilities, should components of the system warrant assessment at very low failure-probability levels. Fundamental definitions of resistance and load statistics follow Nowak and Collins [51]. A comprehensive review of life-cycle performance assessment frameworks for deteriorating structural systems under uncertainty was provided by Biondini and Frangopol [52], establishing the methodological context for the present reliability chain.

The twelve random variables entering the simulation are listed in Table 1 together with their distribution types, moments, and sources.

Table 1. Random variables in the reliability simulation.

No.	Variable	Symbol	Distribution	Mean	CoV	Source
1	Corrosion rate constant	A	Lognormal	75 μm·yr⁻¹	0.30	[24] (field exposure)
2	Time exponent	n	Normal	0.55	0.15	[24] (field exposure)
3	Initial zinc thickness	z_0	Lognormal	85 μm	0.15	Manufacturer spec. (laboratory QC)
4	Zinc consumption rate	r_z	Normal	8.5 μm·yr⁻¹	0.20	[6] (field exposure)
5	Yield strength	f_y	Lognormal	387 MPa	0.07	[51] (laboratory coupon test)
6	Elastic modulus	E	Lognormal	200 GPa	0.03	[51] (laboratory coupon test)
7	50-yr extreme wind speed	V_{50}	Gumbel	38 m·s⁻¹	0.12	Local meteorological record (field)
8	Wind-load model uncertainty	θ_W	Lognormal	1.00	0.10	[51] (field)
9	Dead-load bias factor	δ_G	Normal	1.05	0.04	[51] (laboratory + field survey)
10	Calibration regression error	$\varepsilon_{\mathrm{cal}}$	Normal	0	σ= 0.18 mm	This study(field UT calibration)
11	Segmentation bias	θ_{seg}	Normal	1.00	0.03	This study(validation set, field imagery)
12	Member imperfection	e_0/L	Normal	1/1000	0.33	[47] (laboratory measurement)

2.7. Sobol' Global Sensitivity Analysis

Global sensitivity analysis decomposes the total variance of $\beta(t)$ into contributions attributable to each uncertain input and to interactions among inputs. We adopt the Sobol' variance decomposition [28], in which the first-order index S_i measures the fractional variance explained by input X_i alone, and the total-order index S_{T_i} additionally captures all interaction effects involving X_i. The Saltelli [53] quasi-random estimator with a base sample size of $N_{\text{base}} = 8192$ and $k = 12$ inputs requires $N_{\text{base}} \times (2k + 2) = 213{,}504$ model evaluations. Independent verification is provided by a third-order polynomial chaos expansion (PCE) surrogate trained on 500 Latin hypercube samples, following the methodology of Sudret [54]. The two estimators (Monte Carlo and PCE) are compared to assess convergence and possible bias.

2.8. Alert Classification and Maintenance Optimization

The reliability trajectory $\beta(t)$ is mapped to a four-level alert system calibrated against the target reliability indices in prevailing structural design standards:

1. **Green** ($\beta \geq 4.0$): routine 3-year monitoring cycle.
2. **Yellow** ($3.2 \leq \beta < 4.0$): annual engineering review and increased monitoring frequency.
3. **Orange** ($2.5 \leq \beta < 3.2$): protective recoating and detailed engineering assessment required.
4. **Red** ($\beta < 2.5$): immediate member replacement or load restriction.

Maintenance scheduling seeks to minimize the discounted expected life-cycle cost (LCC) over a specified planning horizon T_H. The life-cycle cost framework follows the formulation pioneered by Frangopol et al. [55] and subsequently refined in a series of studies: Frangopol et al. [56] extended the approach to reliability-based life-cycle management of highway bridges, Kong and Frangopol [57] addressed expected maintenance cost evaluation, and Liu and Frangopol [58] introduced multiobjective optimization balancing condition, safety, and cost. Okasha and Frangopol [59] further developed multicriteria lifetime maintenance planning. The optimization problem is as follows:

$$\min_{t_j, \mathcal{M}_j} C_{\text{LCC}} = \sum_{j=1}^{N_{\text{int}}} \frac{C_{\text{maint},j}}{(1+r)^{t_j}} + \sum_{k=1}^{N_T} \frac{p_f(t_k)\, C_f}{(1+r)^{t_k}} + C_{\text{insp}} \tag{9}$$

subject to $\beta(t) \geq \beta_{\text{target}}$ at all decision epochs, the maintenance optimization in Equation (9) rests on three explicit assumptions about the action set $\mathcal{M}_j$ that deserve to be stated. **(a) Recoating effectiveness.** A protective recoating intervention is modeled as restoring the zinc-equivalent barrier to a fraction κ_recoat of the original coating thickness z_0; in the case study, κ_{recoat} is taken as lognormal with a mean of 0.85 and CoV 0.10, reflecting the imperfect surface preparation typically achievable on in-service members compared with factory hot-dip galvanizing. **(b) Post-intervention deterioration.** After a recoating intervention, corrosion is assumed to re-initiate at a new time $T'_{init} = \frac{\kappa_{recoat} z^0}{r_z}$, with subsequent thickness loss following the same power-law form of Equation (2) and the same posterior on (A, n). A member-replacement intervention resets the member to its as-built state (full t_0, full z_0). **(c) Uncertainty in maintenance actions.** Both κ_{recoat} and the timing of each scheduled intervention carries distributional uncertainty (lognormal κ_recoat as above; ±2 years uniform on intervention timing to reflect routing-and-permit delays); these are sampled within the same Monte Carlo run that produces β(t), so the LCC values are themselves expectations over the joint distribution of intervention quality and timing rather than point estimates conditional on perfectly executed maintenance.

The 71% LCC reduction reported for the selective strategy in Table 5 is benchmarked against blanket intervention. To check whether this number is an artifact of comparing against an operationally extreme baseline, an intermediate strategy—full tower recoating at year 20 and again at year 45, without member replacement—was also evaluated under the same cost parameters; it returned LCC ≈ ¥1420 k and minimum β ≈ 3.4 at year 58, so the selective strategy retains a 46% advantage against this fairer comparator (Section 3.7).

The ranking is also robust to the assumed consequence-of-failure cost: varying C_f between ¥6 M and ¥24 M leaves the selective strategy on top across the whole range, with the gap narrowing to 28% at the low end and widening to 62% at the high end (Section 3.7).

Where $C_{\mathrm{maint},j}$ is the direct cost of intervention $\mathcal{M}_j$ at year t_j, r is the real discount rate, C_f is the consequence-of-failure cost, and C_{insp} is the cumulative inspection cost. Sobol' rankings prioritize interventions on members whose dominant uncertain parameters lie in the distribution's upper tail—operationalizing the value-of-information concept. System-level reliability treats the lattice tower as a series–parallel network in which leg-group redundancy is modeled as a parallel subsystem and the diagonal bracing subsystem is modeled as a series chain. Three features of this series–parallel idealization deserve to be made explicit. **Member interaction.** The series-chain treatment of the diagonal bracing subsystem reflects the empirical observation, supported by the progressive-collapse analyses of Asgarian et al. [10], that loss of a single critical diagonal in a lattice tower can trigger cascading failure of adjacent braces through redistribution of the lost member's force onto neighboring elements that are not themselves designed for that incremental load. The parallel-subsystem treatment of the four-leg group, by contrast, captures the genuine redundancy of the leg system: the loss of one leg does not by itself produce collapse, because the remaining three legs and their bracing can sustain the redistributed vertical load up to a higher limit state. **Load redistribution.** Within each member's individual limit-state evaluation, the demand S(t) is computed assuming the as-designed force distribution; redistribution following a failure event is captured at the system level rather than the member level, by re-evaluating the failure probability of each surviving member conditional on the failed-member subset, and combining these conditional probabilities through the series–parallel network. **System failure mechanisms.** Three failure modes are tracked: (i) tension yielding of any lacing bar, (ii) compression buckling of any diagonal brace, and (iii) loss of leg-group redundancy (defined as failure of any two of the four legs). The system reliability index β_{sys} is then computed from the union probability of these three mode-level events; in the case study, mode (ii)—diagonal-brace buckling—dominates over the full 60-year planning horizon. A more refined treatment that resolves post-buckling load paths and joint-level stress concentrations through a nonlinear finite-element model is acknowledged among the limitations in Section 4 and is the subject of ongoing work.

Bayesian conditioning at each inspection epoch sharpens the posterior estimates over the tower's service life, embodying the adaptive management philosophy advocated by Frangopol [60]. Estes and Frangopol [61] demonstrated that visual-inspection results can meaningfully update bridge reliability estimates within such a framework—a precedent directly transferable to tower fleet management. Kim and Frangopol [62] further showed that structural health monitoring can be optimized on the basis of availability theory to achieve cost-effective lifetime performance.

3. Results

3.1. Study Site and Data Collection

The framework was demonstrated on a 42 m self-supporting galvanized-steel lattice tower located in an ISO 9223 C4 coastal-industrial zone along China's southeastern seaboard [6]. The tower was erected in 1984 and had accumulated approximately 40 years of service at the time of inspection. Primary structural members consist of hot-dip galvanized equal-angle sections: L100 × 100 × 10 mm leg members (Q345B steel), L75 × 75 × 6 mm diagonal braces, and L63 × 63 × 5 mm lacing bars. A DJI Matrice 300 RTK platform (DJI, Shenzhen, China) equipped with a Zenmuse P1 camera (45-megapixel sensor; DJI, Shenzhen, China) acquired 486 images during a clear-sky window in January 2024. Three ArUco fiducial markers installed at representative heights yielded a mean calibration factor of 0.284 mm·pixel $^{-1}$ with a coefficient of variation of 1.2%, confirming sub-pixel geometric consistency.

3.2. Segmentation Performance Evaluation

Table 2 compares the segmentation performance of the two proposed paths against two widely adopted baseline methods on the 400-image held-out validation set. DeepLabV3+ achieved mIoU = 0.913, outperforming the U-Net baseline (mIoU = 0.889) and substantially exceeding the Otsu global thresholding method (mIoU = 0.724). The HSV path attained mIoU = 0.847 at a computational cost roughly five times lower than the deep-learning alternatives.

Table 2. Segmentation performance on the 400-image validation set.

Method	mIoU	Precision	Recall	F1-Score	Inference Time (s·Image^{-1})
Otsu global thresholding	0.724	0.781	0.762	0.771	0.08
HSV thresholding (this study)	0.847	0.893	0.872	0.882	0.27
U-Net with ResNet-34 backbone	0.889	0.921	0.906	0.913	1.42
DeepLabV3+ (this study)	0.913	0.946	0.924	0.935	1.68

Note: Deep-learning inference on NVIDIA RTX 3060 GPU(NVIDIA Corporation, Santa Clara, CA, USA); thresholding methods on Intel i7-12700 CPU(Intel Corporation, Santa Clara, CA, USA).

In Figure 3, the corroded region in the ground-truth annotation (panel b) is highlighted as a red overlay on top of the original UAV photograph, while the HSV and DeepLabV3+ outputs (panels c and d) display corroded pixels in white against a black background representing the intact surface. The boundary of the structural member itself is given by the silhouette of the angle section visible in all four panels.

Qualitative examination of the segmentation maps (Figure 3) revealed two characteristic failure modes of the HSV path: false negatives in shadow zones, where reduced V-channel intensity pushed genuinely corroded pixels below the detection threshold; and false positives on residual zinc patina, whose oxidized surface color falls within the rust hue window. DeepLabV3+ handled both scenarios more robustly owing to its learned contextual features, though it occasionally hallucinated small corrosion patches on bolt-head shadows—a failure mode suppressed by the morphological post-processing step.

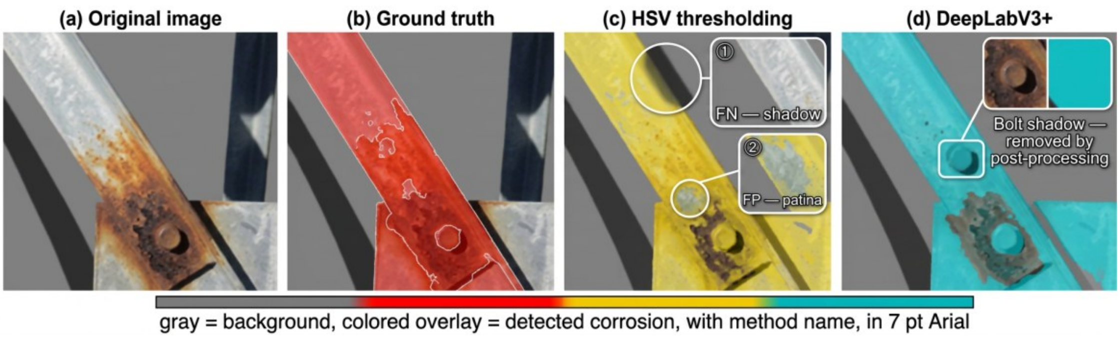

Figure 3. Segmentation comparison on a representative diagonal brace: (**a**) UAV photograph, (**b**) ground-truth annotation, (**c**) HSV output, (**d**) DeepLabV3+ output. Insets highlight characteristic failure modes.

3.3. Section-Loss Calibration and Validation

Corroded area fractions derived from DeepLabV3+ segmentation ranged from 0.02 on sheltered upper-tier leg members to 0.41 on the lowest-panel diagonal braces directly exposed to windborne salt spray. The most severely degraded member—diagonal brace D-7 in the lowest panel—exhibited a calibrated section-loss ratio of $\eta = d/t_0 = 0.28$. Independent ultrasonic thickness measurements at three locations on D-7 returned a mean section-loss ratio of $\eta_{\mathrm{UT}} = 0.26$, confirming the image-based estimate within the measurement uncertainty band (± 0.03).

3.4. Multi-Mode Analysis Comparison

Table 3 summarizes the accuracy of the three analysis modes, evaluated on a subset of 50 members for which ground-truth ultrasonic data and multi-angle imagery were both available.

Table 3. Comparison of the three analysis modes (50-member evaluation subset).

Analysis Mode	Mean Absolute Error (mm)	Outlier Rate (%)	Correlation Coefficient R^2
Mode 1: Single-image	0.24	12.0	0.86
Mode 2: Multi-angle fusion	0.15	2.0	0.94
Mode 3: Temporal differencing	0.13 (rate estimate)	4.0	0.92

Note: Outlier defined as an absolute error exceeding twice the calibration residual standard deviation.

Multi-angle weighted-median fusion reduced the mean absolute error by 38% relative to the single-image mode and suppressed the outlier rate from 12% to 2%. The improvement arises because the weighted-median operator rejects the rare views in which foreshortening, specular reflection, or partial occlusion produce biased estimates. Mode 3, applicable only when historical imagery exists, yielded the tightest rate estimates; the slightly higher outlier rate relative to Mode 2 stems from imperfect homography registration in a small number of image pairs with substantial viewpoint change. The distributions of signed estimation error for the three analysis modes are compared visually in Figure 4.

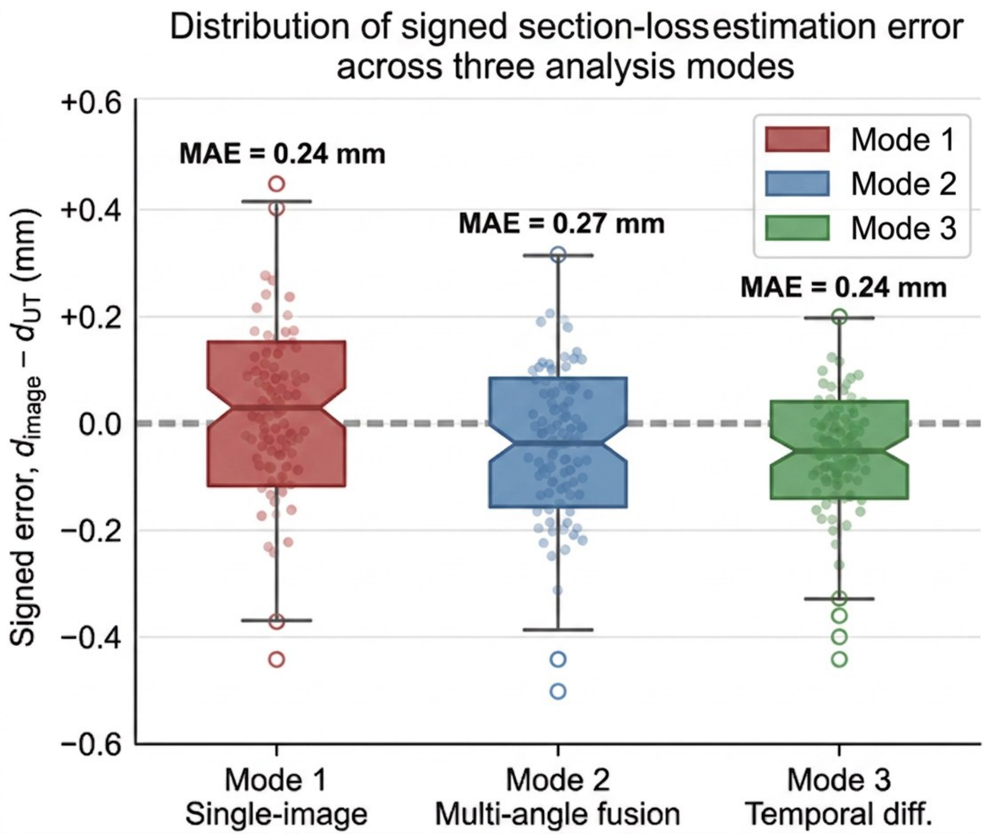

Figure 4. Signed estimation error (image-based minus ultrasonic) for the three analysis modes. Boxes span the interquartile range; whiskers, the 5th–95th percentiles; circles, individual outliers.

3.5. Reliability Index Trajectories

Monte Carlo simulation with 10^6 realizations over a 60-year planning horizon produced the member-level reliability trajectories shown in Figure 5. The most degraded member, diagonal brace D-7, declined from $\beta = 5.1$ at year 0 to $\beta = 2.7$ at year 40 (the current inspection epoch). The median projected crossing of the target threshold $\beta_{target} = 3.0$ occurred at year 43, with the 90% credible interval spanning years 39 to 51. That twelve-year spread quantifies, in operational terms, the consequence of epistemic uncertainty in the corrosion parameters: the difference between “three years until mandatory intervention” and “eleven years of remaining margin.” Leg members, benefiting from their larger cross-sections and the parallel redundancy of the four-leg configuration, retained $\beta > 4.0$ through year 60 even under pessimistic realizations. The system-level reliability index breached $\beta_{target} = 3.0$ at year 44, driven entirely by the diagonal bracing subsystem acting as the series weak link. Three features of Figure 5 deserve closer comment. First, the credible bands widen monotonically with service age, reflecting the cumulative effect of epistemic uncertainty in the corrosion parameters as the prediction horizon lengthens; the band width on D-7 grows from less than 0.4 β-units at year 0 to more than 1.6 β-units at year 60. Second, the curves for leg members and diagonal braces diverge progressively after year 25, even though both member groups experience the same exterior corrosion environment. The divergence is geometrical rather than environmental: legs have a larger cross-section and lower slenderness, so identical thickness loss translates into a much smaller relative loss of buckling capacity. Third, the system curve closely tracks the diagonal-brace median over the entire horizon, confirming that the diagonal subsystem—organized in series at the system level—governs reliability whenever any individual diagonal approaches its limit state. This dominance is consistent with the progressive-collapse findings of Asgarian et al. [10], in which loss of a single critical diagonal triggers cascading bracing failure.

Operationally, the twelve-year spread of the β = 3.0 crossing on D-7 (years 39–51 at 90% credibility) translates directly into maintenance scheduling tolerance: the next inspection must occur no later than year 41 (two years before the lower-bound crossing) to retain the option of a planned, rather than emergency, intervention.

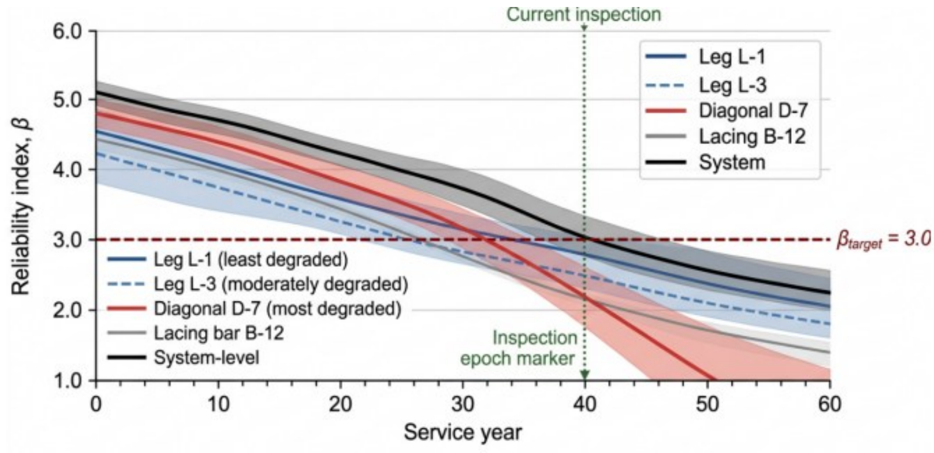

Figure 5. Reliability index β versus service year for selected members and the system. Solid curves, medians; shaded bands, 5th–95th percentile credible intervals. The dashed line marks $\beta_t arget$ = 3.0.

3.6. Sensitivity Decomposition

Table 4 reports the Sobol′ first-order (S_i) and total-order (S_{T_i}) sensitivity indices for β evaluated at year 50, computed by both the Saltelli Monte Carlo estimator and the PCE surrogate.

Table 4. Sobol′ sensitivity indices for the reliability index at year 50.

Variable	S_i (MC)	S_i (PCE)	S_{T_i} (MC)	S_{T_i} (PCE)	Rank
Corrosion rate A	0.381	0.376	0.423	0.418	1
Zinc thickness z_0	0.268	0.271	0.301	0.296	2
Wind speed V_{50}	0.139	0.142	0.156	0.158	3
Wind model uncertainty θ_W	0.067	0.064	0.078	0.075	4
Yield strength f_y	0.058	0.061	0.064	0.067	5
Time exponent n	0.034	0.032	0.048	0.045	6
Remaining 6 variables	0.053	0.054	0.078	0.077	7–12
Sum of S_i	1.000	—	—	—	—

Note: MC = Saltelli estimator (213,504 evaluations); PCE = third-order polynomial chaos expansion (500 LHS training samples). Agreement between the two estimators is within 5%.

The corrosion rate constant A and the zinc coating thickness z_0 collectively account for approximately 65% of the total reliability index variance—corrosion-side uncertainties dominate the outcome by a factor of roughly three over load-side uncertainties. The gap between S_{T_i} and S_i for the corrosion rate (0.423 versus 0.381) reveals an interaction contribution of approximately 4%, attributable primarily to the A–z_0 coupling: fast corrosion combined with thin zinc produces disproportionately severe damage because initiation occurs early and the aggressive post-zinc corrosion phase begins sooner. This nonlinear coupling carries a practical implication for procurement specifications—specifying thicker zinc without controlling the post-initiation corrosion rate yields diminishing reliability returns in the upper tail of the damage distribution. Image-segmentation bias contributes only 1.2% of total variance, confirming that the DeepLabV3+ accuracy far exceeds the precision demanded by the downstream reliability analysis. The complete ranking of total-order sensitivity indices for all twelve random variables is presented graphically in Figure 6.

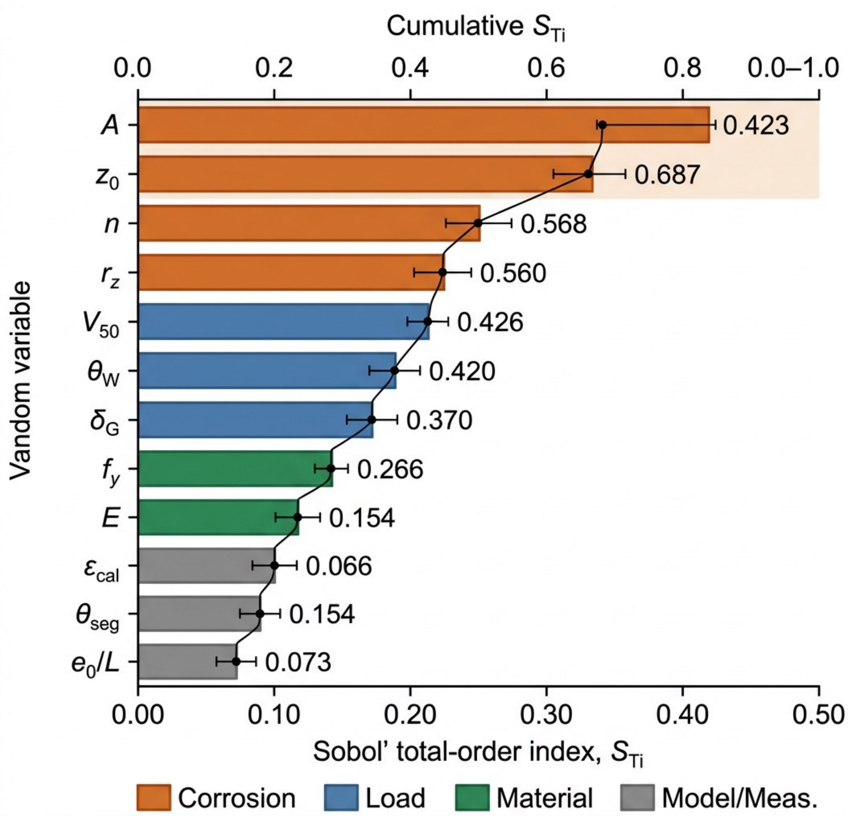

Figure 6. Sobol' total-order indices $S_T i$ for the twelve random variables, grouped by category (corrosion, load, material, model/measurement). Error bars give the 95% bootstrap confidence interval.

3.7. Life-Cycle Cost and Maintenance Strategy Comparison

Three maintenance strategies were evaluated over the 60-year planning horizon, with results summarized in Table 5. The failure consequence cost was set at C_f = ¥12 million (encompassing service outage, emergency repair, and third-party liability), and the real discount rate was 3%.

Table 5. Life-cycle cost comparison for three maintenance strategies (60-year horizon, 2024 CNY).

Item	Do-Nothing	Blanket	Proposed Selective
Year-30 intervention	—	Full recoating (¥640 k)	Replace 8 diagonals + recoat 4 legs (¥328 k)
Year-45 intervention	—	—	Replace 6 lacing bars (¥150 k)
Year-50 intervention	—	Full replacement (¥1800 k)	—
Direct maintenance cost	¥0	¥2440 k	¥478 k
Expected risk cost	¥3870 k	¥0	¥42 k
Inspection cost	¥120 k	¥180 k	¥240 k
Expected total LCC	¥3990 k	¥2620 k	¥760 k
Normalized LCC (% of blanket)	152%	100%	29%
Minimum system β	1.8 (yr 52)	> 4.5	3.2 (yr 44)
Members treated	0	~96 (all)	18 (targeted)

The proposed selective strategy achieves a 71% reduction in expected life-cycle cost relative to the blanket strategy while maintaining the system reliability index above the target threshold throughout the planning horizon. The key enabler is member-level resolution: because the framework identifies precisely which members are critically degraded and which retain ample capacity, the optimizer targets only 18 members for replacement and leaves the remaining 78 untouched. The blanket approach incurs a full tower replacement at year 50 that is entirely unnecessary for the leg members—elements that retain adequate capacity through year 60 under all simulated scenarios. To check whether the selective strategy only looks favorable because the two baselines are operationally extreme—doing nothing versus blanket replacement—we ran a more realistic intermediate case: a full tower recoating at year 20 and again at year 45, with no member replacement. With identical cost parameters, this gave an expected LCC of about ¥1420 k and a minimum β of 3.4 at year 58. That is better than blanket replacement but still 87% more expensive than the selective policy. In other words, the 71% LCC reduction in Table 5 shrinks to 46% against this fairer comparator—but the ordering of the three policies does not change. We also varied C_f *between* ¥6 M and ¥24 M to check the sensitivity of the ranking to the failure-consequence cost. The selective strategy came out on top across the whole range, with the gap narrowing to 28% at C_f = ¥6 M and widening to 62% at C_f = ¥24 M. The breakdown of life-cycle cost components under the three strategies is compared in Figure 7, and the corresponding system reliability index trajectories over the 60-year planning horizon are plotted in Figure 8.

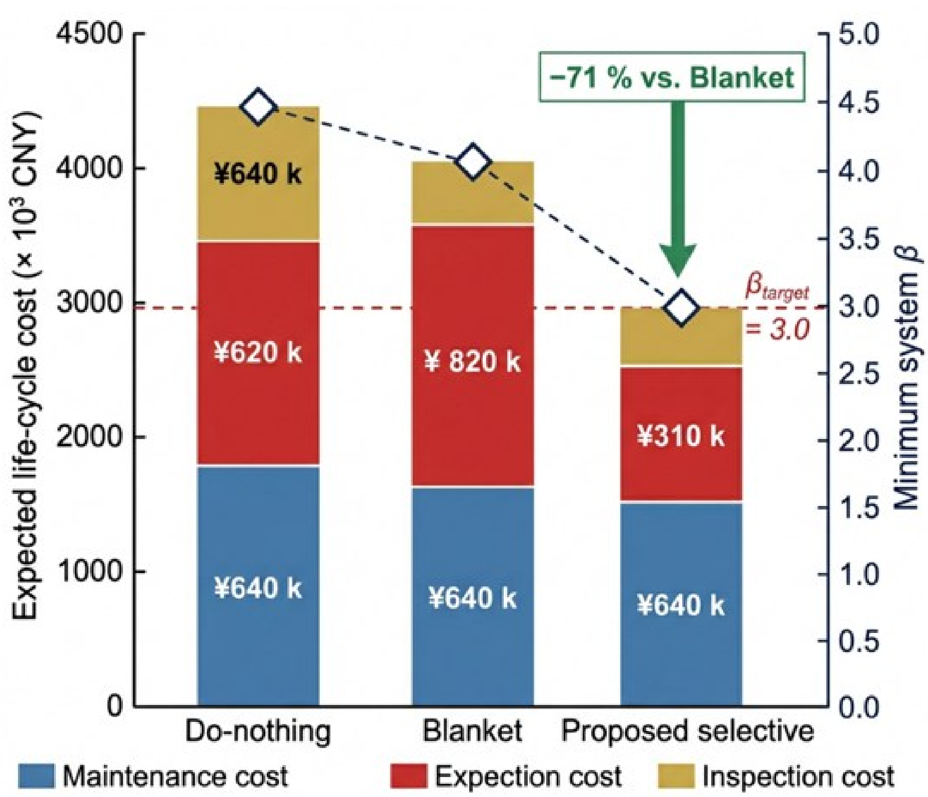

Figure 7. Life-cycle cost components for the three maintenance strategies (stacked bars). Diamond markers on the right axis show the minimum system β achieved under each strategy.

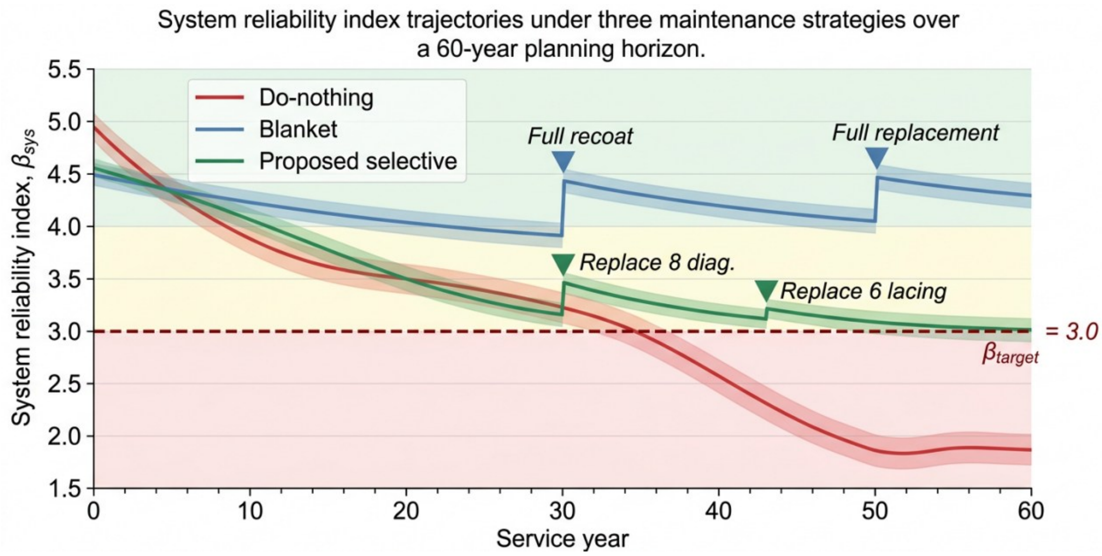

Figure 8. System reliability index trajectories under the three maintenance strategies over the 60-year horizon. Arrows mark intervention epochs; the dashed line marks β_target = 3.0.

4. Discussion

The results of the field demonstration carry several implications that merit discussion before drawing conclusions.

The dominance of corrosion-side parameters (A and z_0, collectively 65% of variance) over load-side parameters (V_{50} and θ_W, collectively 23%) provides a quantitative basis for monitoring-budget allocation. In practical terms, investing in more precise characterization of the corrosion environment and coating quality—through coupon exposure programs, coating thickness surveys, or environmental sensor networks—is roughly three times more effective at reducing decision uncertainty than refining wind-load estimates. This ranking aligns with the broader finding in the life-cycle management literature that resistance-side uncertainties tend to dominate aging infrastructure [52,60], but it has not previously been quantified for steel tower structures with field-measured corrosion inputs. A further implication of this ranking concerns the design stage itself. Conventional tower design devotes considerable analytical effort to wind-load characterization—gust factors, terrain categories, dynamic amplification—because wind has historically been treated as the dominant uncertain action. The Sobol′ decomposition reported here suggests that, for towers intended to operate for 40 years or more in aggressive atmospheric environments, the marginal reliability return on further wind-load refinement is modest compared with the return on tighter control of corrosion-side variables. From an engineer's perspective, this points toward two design-stage adjustments: (i) corrosion-protection specifications (zinc coating thickness, supplemental barrier coatings, alloy selection) should be calibrated against the site's measured corrosivity rather than its nominal ISO 9223 class, treating coating thickness as a primary design variable rather than a code-mandated minimum; and (ii) inspection intervals, member-replacement triggers, and recoating schedules should be embedded in the original design package, with the structure's whole-life reliability—not its day-one reliability—as the design target. This shift from one-time design to lifetime design is consistent with emerging life-cycle engineering frameworks [52,60] and is operationally enabled by the assessment chain demonstrated in this paper.

The interaction effect between A and z_0, though modest in aggregate (approximately 4% of total variance), reveals a nonlinear coupling with significant procurement implications. Specifying a thicker zinc coating shifts the initiation time rightward, but if the post-initiation corrosion rate is not simultaneously controlled through, for example, alloy selection or supplemental barrier coatings—the reliability gain saturates and eventually diminishes at the upper tail of the damage distribution. This observation suggests that hot-dip galvanizing specifications should be paired with environmental-corrosivity audits when towers are sited in aggressive C4 or C5 atmospheres.

An additional implication concerns the integration of ambient air-quality data into the framework. The power-law growth model in Section 2.5 enters the pipeline through its prior on (A, n), which is currently parameterized from ISO 9223 corrosivity classes. Because the framework is modular, this prior can be replaced—without altering any downstream module—by an environment-aware regression in which A is expressed as a function of measured SO_2, NO_2, PM_{10}, chloride deposition rate, and time-of-wetness drawn from co-located air-quality monitoring stations. For towers instrumented with environmental sensors, or those located within the coverage of municipal air-quality networks, this substitution is operationally trivial and would tighten the prior on the corrosion rate constant before the first inspection update is even applied. Validation of such an environment-aware prior across multiple Chinese coastal-industrial sites is part of our ongoing work.

From the standpoint of inspection operations, the dual-path segmentation strategy reconciles two conflicting requirements. Fleet-level triage demands speed: the HSV path processes a full tower's image set in under three minutes and flags members exceeding a user-defined area-fraction threshold for deeper analysis. Detailed engineering assessment demands accuracy: the DeepLabV3+ path, though six times slower, delivers an mIoU of 0.913 that translates into a segmentation-bias contribution of only 1.2% to the total reliability-index variance. Deploying both paths in sequence—screen first, quantify second—matches the staged decision architecture that most asset managers already follow intuitively but lack the quantitative tools to implement.

Multi-angle fusion should be the default analysis mode whenever flight time permits multiple viewpoints per member. The 38% reduction in mean absolute error relative to single-image analysis costs only modest additional field time and proceeds automatically. The weighted-median aggregation is inherently robust to the occasional aberrant view caused by specular glare or motion blur—a practical advantage over simple averaging.

A note on the practical validation of the integrated framework is in order. The individual modules of the pipeline are each anchored to an independent measurement: the segmentation module against pixel-level ground-truth annotations on a 400-image held-out validation set (Table 2), the image-to-thickness calibration regression against contact ultrasonic gauging on 120 member faces (Equation (1), Figure 2), the most severely degraded member's image-derived section-loss against direct ultrasonic measurement at three locations on the same member (Section 3.3, $\eta = 0.28$ by image versus $\eta_{UT} = 0.26$ by ultrasonics), and the analytical member forces against a linear-elastic finite-element model of the case-study tower under the governing wind case (8% agreement, Section 4 limitations). What is currently missing—and what would constitute the ideal closing of the validation loop—is a comparison of the framework's reliability predictions and maintenance recommendations against multi-decade historical inspection, repair, and replacement records on the same or a comparable tower. Such records do not exist for the case-study structure, because routine inspection on this tower has, like elsewhere in the field, used categorical visual grading rather than quantitative thickness logging. Constructing a longitudinal record by repeating the present UAV-based inspection protocol at three- to five-year intervals on the case-study tower, and on a broader fleet, is therefore the most direct path to full-workflow validation; this is part of our ongoing work and is acknowledged among the limitations below.

Four limitations of the present work deserve explicit acknowledgment.

First, the area-fraction-to-depth calibration (Equation (1)) derives from 120 member faces on a single tower type composed of equal-angle galvanized sections in a C4 coastal-industrial environment; its transferability to (i) other section types—tubular, channel, wide-flange—(ii) other corrosion morphologies, particularly heavily pit-clustered surfaces that do not appear in the calibration set, and (iii) other corrosivity environments, particularly C5 industrial or CX tropical-marine, has not been validated. A leave-one-member-out re-fit of the regression on the calibration set returned coefficient standard errors of 0.21 mm on α and 0.06 on γ, with no individual member dominating the fit, indicating that the present coefficients are internally stable; this is not, however, a substitute for cross-section-specific or cross-environment recalibration. We therefore recommend that any application of Equation (1) outside the equal-angle/C4 envelope of the present study be preceded by a section-specific calibration campaign of at least 30–50 member faces with paired image and ultrasonic measurements, following the same protocol described in Section 2.4. Hierarchical Bayesian re-fitting that pools across multiple section types while preserving section-specific coefficients is one path to make this recalibration data-efficient and is part of our ongoing work.

Second, uniform-thickness-loss modeling is known to underestimate capacity reduction on compression members, where pit-induced stress concentrations interact with buckling instability [25,47]. The elevated alert thresholds introduced in Section 2.6 absorb part of this optimism, but a cleaner treatment would couple the power-law depth model with a stochastic pit-distribution model such as the one in Valor et al. [33]. Compression-member reliability indices in this study should therefore be taken as upper bounds, and the selective maintenance schedule derived from them as a lower bound on what the structure will eventually need.

Third, the study demonstrates the framework on one structure only; generalization across tower populations would benefit from hierarchical Bayesian models that share strength across sites while preserving local variability, in the spirit of the bridge-fleet approach demonstrated by Estes and Frangopol [61].

Fourth, member resistances in this work come from analytical column-curve and tension-yield equations (Section 2.6), not from a nonlinear finite-element model of the lattice. Stress redistribution in redundant zones, secondary bending at joints, and post-buckling load paths enter the reliability calculation only through the series–parallel idealization at the system level. A linear-elastic FE check on the case-study tower reproduced the analytical axial forces in the critical diagonal braces to within about 8% under the governing wind case, which is adequate for fleet-scale screening. Pushing the framework to ultimate-limit-state certification on individual towers will require a nonlinear FE model that resolves post-buckling and joint-level stress concentrations, and that work is ongoing.

5. Conclusions

An integrated, multi-mode framework has been developed for image-based corrosion assessment and reliability-informed maintenance planning of steel tower structures. The principal findings and contributions are summarized as follows.

A dual-path segmentation strategy pairs a fast HSV thresholding detector (mIoU = 0.847, 0.27 s per image) with a high-accuracy DeepLabV3+ semantic segmentation model (mIoU = 0.913, 1.68 s per image), providing quantitative corrosion mapping that supersedes subjective categorical grading. The two paths are linked to structural section loss through a calibrated nonlinear regression with a residual standard deviation of 0.18 mm.

Three analysis modes accommodate diverse inspection scenarios. Multi-angle weighted-median fusion reduces section-loss estimation error by 38% relative to single-image analysis while suppressing the outlier rate from 12% to 2%. Temporal differencing via ORB-feature matching extracts empirical corrosion rates for direct model updating.

Monte Carlo simulation with 10^6 realizations and Bayesian-updated growth parameters projects the most severely degraded diagonal brace to breach the target reliability index $\beta = 3.0$ within approximately three years of the current inspection epoch, though the 90% credible interval extends from year 39 to year 51 of service—a spread that quantifies the practical consequence of epistemic uncertainty in the corrosion parameters.

Sobol' variance decomposition identifies the first-year corrosion rate constant and the initial zinc coating thickness as the dominant uncertainty drivers, together accounting for 65% of the total reliability-index variance. Corrosion-side uncertainties outweigh load-side uncertainties by a factor of three, providing a quantitative rationale for prioritizing corrosion-environment and coating characterization in monitoring budgets.

A risk-ranked selective maintenance strategy targeting only the 18 most critically degraded members reduces expected life-cycle cost by 71% relative to blanket intervention, while maintaining the system reliability index above the target throughout a 60-year planning horizon.

The findings reported above derive from a single field demonstration on one 40-year-old galvanized lattice tower in a C4 coastal-industrial environment. The numerical values—the 65% combined variance contribution of A and z_0, the 71% life-cycle cost reduction, the year-43 median crossing of $\beta = 3.0$—should therefore be read as quantitatively representative of this specific structure and environment, not as universal benchmarks. The qualitative conclusions of the study are expected to generalize: corrosion-side parameters are likely to dominate over load-side parameters in aging steel towers across most C3–C5 environments, and risk-ranked selective maintenance is likely to outperform blanket replacement in most asset portfolios. However, the absolute magnitudes of the savings and the specific Sobol' rankings are sensitive to environmental aggressiveness, original coating quality, member section type, and the tower's structural redundancy. Caution is therefore warranted when transferring the numerical conclusions to towers of substantially different age, geometry, or exposure category. Cross-population validation through hierarchical Bayesian models, as outlined below, is the next step to convert the present case-study evidence into a fleet-level decision tool.

Future work will pursue three extensions: incorporating spatially heterogeneous corrosion fields via finite-element surrogates to relax the uniform-loss assumption; validating the framework across tower populations spanning multiple corrosivity categories through hierarchical Bayesian modeling; and developing a field-deployable real-time asset management dashboard that integrates the data-acquisition, analysis, and decision layers into a unified software platform.

Author Contributions: Conceptualization, H.Z. and D.H.; methodology, H.Z. and C.Y.; software, H.Z. and Y.C.; validation, J.C. and D.H.; formal analysis, H.Z.; investigation, H.Z. and Y.C.; resources, D.H.; data curation, H.Z. and J.C.; writing—original draft preparation, H.Z.; writing—review and editing, C.Y. and D.H.; visualization, H.Z.; supervision, D.H.; project administration, D.H.; funding acquisition, D.H. All authors have read and agreed to the published version of the manuscript.

Funding: This research received no external funding.

Data Availability Statement: The computational pipeline was implemented in Python 3.12.10, using standard open-source libraries for deep learning (PyTorch 2.7.1), image processing (OpenCV 4.13.0), scientific computing (SciPy 1.16.3), Bayesian inference (PyMC 5.16), and global sensitivity analysis (SALib 1.5.1); deep-learning training and inference were performed on an NVIDIA RTX 3060 GPU. Library versions, training hyperparameters, and Monte Carlo settings are reported in Sections 2.3.2, 2.5–2.7 of the manuscript and are sufficient to reproduce the analysis. The image dataset, pretrained DeepLabV3+ model weights, annotation files, and evaluation scripts used in this study are available from the corresponding author upon reasonable request, subject to the asset owner's image-release policy.

Conflicts of Interest: The authors declare no conflicts of interest.

References

1. Koch, G.H.; Brongers, M.P.H.; Thompson, N.G.; Virmani, Y.P.; Payer, J.H. *Corrosion Cost and Preventive Strategies in the United States*; Report No. FHWA-RD-01-156; Federal Highway Administration: McLean, VA, USA, 2002.
2. Cole, I.S.; Paterson, D.A. Possible Effects of Air Pollutants and Climate Change on Atmospheric Corrosion. *Corros. Eng. Sci. Technol.* **2010**, *45*, 19–26.
3. Morcillo, M.; Chico, B.; Díaz, I.; Cano, H.; de la Fuente, D. Atmospheric Corrosion Data of Weathering Steels: A Review. *Corros. Sci.* **2013**, *77*, 6–24.
4. Di Sarno, L.; Majidian, A.; Karagiannakis, G. The Effect of Atmospheric Corrosion on Steel Structures: A State-of-the-Art and Case-Study. *Buildings* **2021**, *11*, 571.
5. Mendoza-Rangel, J.M.; Castorena-González, J.H.; Almeraya-Calderón, F.; Gaona-Tiburcio, C. Atmospheric Corrosion of Galvanized Steel in Different Environments: An Update. *Materials* **2023**, *16*, 1502.
6. *ISO 9223:2012*; Corrosion of Metals and Alloys—Corrosivity of Atmospheres—Classification, Determination and Estimation. International Organization for Standardization: Geneva, Switzerland, 2012.
7. Peyrot, A.H.; Dagher, H.J. Reliability-Based Design of Transmission Lines. *J. Struct. Eng.* **1984**, *110*, 2758–2777.
8. Alam, M.J.; Santhakumar, A.R. Reliability Analysis and Full-Scale Testing of Transmission Tower. *J. Struct. Eng.* **1996**, *122*, 338–344.
9. Fu, X.; Li, H.N.; Li, G. Fragility Analysis of Wind-Induced Collapse of a Transmission Tower Considering Corrosion. *Buildings* **2022**, *12*, 1500.
10. Asgarian, B.; Eslamlou, S.D.; Zaghi, A.E.; Mehr, M. Progressive Collapse Analysis of Power Transmission Towers. *J. Constr. Steel Res.* **2016**, *123*, 31–40.
11. Fu, X.; Li, H.N.; Tian, L.; Wang, J.; Cheng, H. Fragility Analysis of Transmission Line Subjected to Wind Loading. *J. Perform. Constr. Facil.* **2019**, *33*, 04019044.
12. Yang, S.C.; Liu, T.J.; Hong, H.P. Reliability of Tower and Tower-Line Systems under Spatiotemporally Varying Wind or Earthquake Loads. *J. Struct. Eng.* **2017**, *143*, 04017137.
13. Agdas, D.; Rice, J.A.; Martinez, J.R.; Lasa, I.R. Comparison of Visual Inspection and Structural-Health Monitoring as Bridge Condition Assessment Methods. *J. Perform. Constr. Facil.* **2016**, *30*, 04015049.
14. Feroz, S.; Abu Dabous, S. UAV-Based Remote Sensing Applications for Bridge Condition Assessment. *Remote Sens.* **2021**, *13*, 1809.
15. Chen, S.; Laefer, D.F.; Mangina, E.; Zolanvari, S.M.I.; Byrne, J. UAV Bridge Inspection through Evaluated 3D Reconstructions. *J. Bridge Eng.* **2019**, *24*, 04019015.
16. LeCun, Y.; Bengio, Y.; Hinton, G. Deep Learning. *Nature* **2015**, *521*, 436–444.
17. Cha, Y.-J.; Choi, W.; Büyüköztürk, O. Deep Learning-Based Crack Damage Detection Using Convolutional Neural Networks. *Comput.-Aided Civ. Infrastruct. Eng.* **2017**, *32*, 361–378.
18. Khayatazad, M.; De Pue, L.; De Waele, W. Detection of Corrosion on Steel Structures Using Automated Image Processing. *Dev. Built Environ.* **2020**, *3*, 100022.
19. Forkan, A.R.M.; Kang, Y.-B.; Jayaraman, P.P.; Liao, K.; Kaul, R.; Morgan, G.; Ranjan, R.; Sinha, S. CorrDetector: A Framework for Structural Corrosion Detection from Drone Images Using Ensemble Deep Learning. *Expert Syst. Appl.* **2022**, *193*, 116461.
20. Bolton, T.; Bastas, A. A Comprehensive Survey of Deep Learning Approaches for Steel Corrosion Detection. *Appl. Sci.* **2024**, *14*, 8044.
21. Spencer, B.F.; Hoskere, V.; Narazaki, Y. Advances in Computer Vision-Based Civil Infrastructure Inspection and Monitoring. *Engineering* **2019**, *5*, 199–222.
22. Rahman, A.; Wu, Z.Y.; Kalfarisi, R. Semantic Deep Learning Integrated with RGB Feature-Based Rule Optimization for Facility Surface Corrosion Detection and Evaluation. *J. Comput. Civ. Eng.* **2021**, *35*, 04021018.
23. Albrecht, P.; Hall, T.T. Atmospheric Corrosion Resistance of Structural Steels. *J. Mater. Civ. Eng.* **2003**, *15*, 2–24.
24. Klinesmith, D.E.; McCuen, R.H.; Albrecht, P. Effect of Environmental Conditions on Corrosion Rates. *J. Mater. Civ. Eng.* **2007**, *19*, 121–129.

25. Melchers, R.E. The Effect of Corrosion on the Structural Reliability of Steel Offshore Structures. *Corros. Sci.* **2005**, *47*, 2391–2410.
26. Ditlevsen, O.; Madsen, H.O. *Structural Reliability Methods*; Wiley: Chichester, UK, 1996.
27. Ellingwood, B.R. Risk-Informed Condition Assessment of Civil Infrastructure: State of Practice and Research Issues. *Struct. Infrastruct. Eng.* **2005**, *1*, 7–18.
28. Sobol', I.M. Global Sensitivity Indices for Nonlinear Mathematical Models and Their Monte Carlo Estimates. *Math. Comput. Simul.* **2001**, *55*, 271–280.
29. Saltelli, A.; Ratto, M.; Andres, T.; Campolongo, F.; Cariboni, J.; Gatelli, D.; Saisana, M.; Tarantola, S. *Global Sensitivity Analysis: The Primer*; Wiley: Chichester, UK, 2008.
30. Kayser, J.R.; Nowak, A.S. Reliability of Corroded Steel Girder Bridges. *Struct. Saf.* **1989**, *6*, 53–63.
31. Czarnecki, A.A.; Nowak, A.S. Time-Variant Reliability Profiles for Steel Girder Bridges. *Struct. Saf.* **2008**, *30*, 49–64.
32. Wang, H.; Tang, F.; Qin, S.; Tu, K.; Guo, J. Corrosion-Induced Mechanical Degradation of High-Strength Bolted Steel Connection. *J. Mater. Civ. Eng.* **2020**, *32*, 04020200.
33. Valor, A.; Caleyo, F.; Alfonso, L.; Velázquez, J.C.; Hallen, J.M. Stochastic Modeling of Pitting Corrosion: A New Model for Initiation and Growth of Multiple Corrosion Pits. *Corros. Sci.* **2007**, *49*, 559–579.
34. Otsu, N. A Threshold Selection Method from Gray-Level Histograms. *IEEE Trans. Syst. Man Cybern.* **1979**, *9*, 62–66.
35. Chen, L.-C.; Zhu, Y.; Papandreou, G.; Schroff, F.; Adam, H. Encoder-Decoder with Atrous Separable Convolution for Semantic Image Segmentation. In *Proceedings of the European Conference on Computer Vision (ECCV), Munich, Germany, 8–14 September 2018*; Springer: Cham, Switzerland, 2018; pp. 801–818.
36. Tan, M.; Le, Q.V. EfficientNet: Rethinking Model Scaling for Convolutional Neural Networks. In Proceedings of the International Conference on Machine Learning (ICML), Long Beach, CA, USA, 9–15 June 2019; pp. 6105–6114.
37. Deng, J.; Dong, W.; Socher, R.; Li, L.-J.; Li, K.; Fei-Fei, L. ImageNet: A Large-Scale Hierarchical Image Database. In Proceedings of the IEEE Conference on Computer Vision and Pattern Recognition (CVPR), Miami, FL, USA, 20–25 June 2009; pp. 248–255.
38. Long, J.; Shelhamer, E.; Darrell, T. Fully Convolutional Networks for Semantic Segmentation. In Proceedings of the IEEE Conference on Computer Vision and Pattern Recognition (CVPR), Boston, MA, USA, 7–12 June 2015; pp. 3431–3440.
39. Ronneberger, O.; Fischer, P.; Brox, T. U-Net: Convolutional Networks for Biomedical Image Segmentation. In Proceedings of the Medical Image Computing and Computer-Assisted Intervention (MICCAI), Munich, Germany, 5–9 October 2015; Springer: Cham, Switzerland, 2015; pp. 234–241.
40. He, K.; Zhang, X.; Ren, S.; Sun, J. Deep Residual Learning for Image Recognition. In Proceedings of the IEEE Conference on Computer Vision and Pattern Recognition (CVPR), Las Vegas, NV, USA, 27–30 June 2016; pp. 770–778.
41. Zhao, H.; Shi, J.; Qi, X.; Wang, X.; Jia, J. Pyramid Scene Parsing Network. In Proceedings of the IEEE Conference on Computer Vision and Pattern Recognition (CVPR), Honolulu, HI, USA, 21–26 July 2017; pp. 2881–2890.
42. Der Kiureghian, A.; Ditlevsen, O. Aleatory or Epistemic? Does It Matter? *Struct. Saf.* **2009**, *31*, 105–112.
43. Straub, D. Stochastic Modeling of Deterioration Processes through Dynamic Bayesian Networks. *J. Eng. Mech.* **2009**, *135*, 1089–1099.
44. Straub, D.; Der Kiureghian, A. Bayesian Network Enhanced with Structural Reliability Methods: Methodology. *J. Eng. Mech.* **2010**, *136*, 1248–1258.
45. Straub, D.; Papaioannou, I. Bayesian Updating with Structural Reliability Methods. *J. Eng. Mech.* **2015**, *141*, 04014134.
46. Li, M.; Jia, G. Bayesian Updating of Bridge Condition Deterioration Models Using Complete and Incomplete Inspection Data. *J. Bridge Eng.* **2020**, *25*, 04020007.
47. Rahgozar, R. Remaining Capacity Assessment of Corrosion Damaged Beams Using Minimum Curves. *J. Constr. Steel Res.* **2009**, *65*, 299–307.
48. *ISO 2394:2015*; General Principles on Reliability for Structures. International Organization for Standardization: Geneva, Switzerland, 2015.
49. *EN 1990:2002*; Eurocode—Basis of Structural Design. European Committee for Standardization (CEN): Brussels, Belgium, 2002.
50. Au, S.-K.; Beck, J.L. Estimation of Small Failure Probabilities in High Dimensions by Subset Simulation. *Probab. Eng. Mech.* **2001**, *16*, 263–277.
51. Nowak, A.S.; Collins, K.R. *Reliability of Structures*, 2nd ed.; CRC Press: Boca Raton, FL, USA, 2013.
52. Biondini, F.; Frangopol, D.M. Life-Cycle Performance of Deteriorating Structural Systems under Uncertainty: Review. *J. Struct. Eng.* **2016**, *142*, F4016001.
53. Saltelli, A. Making Best Use of Model Evaluations to Compute Sensitivity Indices. *Comput. Phys. Commun.* **2002**, *145*, 280–297.
54. Sudret, B. Global Sensitivity Analysis Using Polynomial Chaos Expansions. *Reliab. Eng. Syst. Saf.* **2008**, *93*, 964–979.

55. Frangopol, D.M.; Lin, K.-Y.; Estes, A.C. Life-Cycle Cost Design of Deteriorating Structures. *J. Struct. Eng.* **1997**, *123*, 1390–1401.
56. Frangopol, D.M.; Kong, J.S.; Gharaibeh, E.S. Reliability-Based Life-Cycle Management of Highway Bridges. *J. Comput. Civ. Eng.* **2001**, *15*, 27–34.
57. Kong, J.S.; Frangopol, D.M. Evaluation of Expected Life-Cycle Maintenance Cost of Deteriorating Structures. *J. Struct. Eng.* **2003**, *129*, 682–691.
58. Liu, M.; Frangopol, D.M. Multiobjective Maintenance Planning Optimization for Deteriorating Bridges Considering Condition, Safety, and Life-Cycle Cost. *J. Struct. Eng.* **2005**, *131*, 833–842.
59. Okasha, N.M.; Frangopol, D.M. Novel Approach for Multicriteria Optimization of Life-Cycle Preventive and Essential Maintenance of Deteriorating Structures. *J. Struct. Eng.* **2010**, *136*, 1009–1022.
60. Frangopol, D.M. Life-Cycle Performance, Management, and Optimisation of Structural Systems under Uncertainty. *Struct. Infrastruct. Eng.* **2011**, *7*, 389–413.
61. Estes, A.C.; Frangopol, D.M. Updating Bridge Reliability Based on Bridge Management Systems Visual Inspection Results. *J. Bridge Eng.* **2003**, *8*, 374–382.
62. Kim, S.; Frangopol, D.M. Cost-Effective Lifetime Structural Health Monitoring Based on Availability. *J. Struct. Eng.* **2011**, *137*, 22–33.

https://doi.org/10.3390/buildings16112250